

# INTERACTION OF MASSIVE BLACK HOLE BINARIES WITH THEIR STELLAR ENVIRONMENT: III. SCATTERING OF BOUND STARS

ALBERTO SESANA<sup>1</sup>, FRANCESCO HAARDT<sup>1\*</sup>, & PIERO MADAU<sup>2</sup>

*Submitted to ApJ*

## ABSTRACT

We develop a formalism for studying the dynamics of massive black hole binaries embedded in gravitationally-bound stellar cusps, and study the binary orbital decay by three-body interactions, the impact of stellar slingshots on the density profile of the inner cusp, and the properties of the ejected hyper-velocity stars (HVSs). We find that the scattering of bound stars shrinks the binary orbit and increases its eccentricity more effectively than that of unbound ambient stars. Binaries with initial eccentricities  $e \gtrsim 0.3$  and/or unequal-mass companions ( $M_2/M_1 \lesssim 0.1$ ) can decay by three-body interactions to the gravitational wave emission regime in less than a Hubble time. The stellar cusp is significantly eroded, and cores as shallow as  $\rho \propto r^{-0.7}$  may develop from a pre-existing singular isothermal density profile. A population of HVSs is ejected in the host galaxy halo, with a total mass  $\sim M_2$ . We scale our results to the scattering of stars bound to Sgr A\*, the massive black hole in the Galactic Center, by an inspiraling companion of intermediate mass. Depending on binary mass ratio, eccentricity, and initial slope of the stellar cusp, a core of radius  $\sim 0.1$  pc typically forms in 1-10 Myr. On this timescale about 500-2500 HVSs are expelled with speeds sufficiently large to escape the gravitational potential of the Milky Way.

*Subject headings:* black hole physics – methods: numerical – stellar dynamics

## 1. INTRODUCTION

In the standard paradigm of cosmic structure formation, it is expected that many wide massive black hole binaries (MBHBs) will form following the mergers of two massive galaxies (e.g. Begelman, Blandford, & Rees 1980; Volonteri, Haardt, & Madau 2003; Mayer et al. 2007). The binary will subsequently shrink due to stellar or gas dynamical processes and may ultimately coalesce by emitting a burst of gravitational waves. It was first proposed by Ebisuzaki, Makino, & Okumura (1991) that the heating of the surrounding stars by a decaying SMBH pair would create a low-density core out of a preexisting cuspy (e.g.  $\rho \propto r^{-2}$ ) stellar profile. In a purely stellar background a ‘hard’ binary shrinks by capturing the stars that pass close to the holes and ejecting them at much higher velocities, a super-elastic scattering process (‘gravitational slingshot’) that depletes the nuclear region. Observationally, there is clear evidence in early-type galaxies for a systematically different distribution of surface brightness profiles, with faint ellipticals showing steep power-law profiles (cusps), while bright ellipticals have much shallower stellar cores (e.g. Faber et al. 1997; Ravindranath et al. 2001). Detailed N-body simulations have confirmed the cusp-disruption effect of a hardening MBHB (Makino & Ebisuzaki 1996; Quinlan & Hernquist 1997; Milosavljevic & Merritt 2001), while semi-analytic modelling in the framework of hierarchical structure formation theories has shown that the cumulative damage done to a stellar cusps by decaying black hole pairs may explain the observed correlation between the ‘mass deficit’ (the mass needed to bring a flat inner density profile to a  $r^{-2}$  cusp) and the mass of the nuclear black hole (Volonteri, Madau, & Haardt 2003).

This is the third paper of a series aimed at the detailed study of the interaction between MBHBs and their stellar

environment. In Sesana, Haardt, & Madau (2006, 2007a, hereafter Paper I and Paper II), we analyzed the three-body scatterings between a MBHB and background stars *unbound* to the binary. The assumption of a fixed background breaks down once the binary has ejected most of the stars on intersecting orbits, and the extraction of energy and angular momentum from the binary can continue only if new stars can diffuse into low-angular momentum orbits (refilling the binary’s phase-space ‘loss cone’), or via gas processes. In galaxies with inner cores or shallow cusps, only a small fraction of the loss cone is confined within the sphere of influence of the binary, and the approximation of a background of unbound stars is reasonable. A similar argument holds also in the case of a galaxy with a steep cusp hosting a nearly equal-mass binary ( $M_1 \sim M_2$ ). The radius of influence of such a pair,  $r_{\text{inf}} = G(M_1 + M_2)/(2\sigma^2)$  where  $\sigma$  is the stellar velocity dispersion, is of the order of the binary hardening radius,  $a_h = GM_2/4\sigma^2$ , and only few low-angular momentum stars have orbits with semi-major axis  $\lesssim r_{\text{inf}}$ . This is not true for unequal-mass binaries, where  $r_{\text{inf}} \gg a_h$ , and almost all interacting stars are bound to  $M_1$ .

In this paper we develop a formalism for studying the dynamics of MBHBs embedded in gravitationally-bound stellar cusps. The plan is as follows. In § 2 we describe our suite of three-body scattering experiments between the black hole pair and ambient bound stars. Our numerical results are used in § 3 and § 4 to construct a ‘hybrid model’ of binary dynamics and investigate the orbital decay and shrinking of MBHBs in time-evolving stellar cusps. The properties of the ejected HVSs are discussed in § 5. The massive black hole (Sgr A\*) in the Galactic Center and the stars around it offer a unique opportunity to study stellar dynamics in the extreme environment around a rel-

<sup>1</sup>Dipartimento di Scienze, Università dell’Insubria, via Valleggio 11, 22100 Como, Italy. \*Affiliated to INFN, Italy.

<sup>2</sup>Department of Astronomy & Astrophysics, University of California, 1156 High Street, Santa Cruz, CA 95064.

ativistic potential. The scattering of stars bound to Sgr A\* by an inspiraling intermediate-mass black hole (IMBH) is treated in § 6. Finally, we present a brief summary in § 7.

## 2. SCATTERING EXPERIMENTS WITH BOUND STARS

Consider a MBH of mass  $M_1$  surrounded by a stellar cusp (with density profile  $\rho \propto r^{-\gamma}$ ,  $\gamma > 0$ ), interacting with a secondary “intruder” hole of mass  $M_2 < M_1$ . As the binary separation decays, the effectiveness of dynamical friction slowly declines because distant stars perturb the binary’s center of mass but not its semi-major axis. The bound pair then loses orbital energy by capturing ambient stars and ejecting them at much higher velocities, a three-body scattering process known as the ‘gravitational slingshot’. For unequal-mass binaries (mass ratio  $q \lesssim 0.1$ ),  $a_h \ll r_{\text{inf}}$ , implying that the stellar mass inside  $a_h$  is  $M_{\text{cusp}}(< a_h) \ll M_1$ . In this case, the contribution to the potential energy given by the stellar distribution during a binary-star interaction can be ignored, and the problem can be tackled by means of three-body scattering experiments. Following the guidelines fully described in Paper I, we performed numerical experiments to study the interaction of a MBHB with a star of mass  $m_*$  ( $m_* \ll M_2 < M_1$ ) bound to  $M_1$ . Note that, for extreme mass ratios  $q \ll 1$ , the encounter is essentially a two-body scattering as the star and the secondary hole move in the static potential of the primary.

### 2.1. Initial conditions and orbit integration

The integration of the three-body encounter equations is greatly simplified by setting the center of mass of the binary at rest in the origin of the coordinate system. The binary orbits counterclockwise in the  $(x, y)$  plane, and the apoastron of  $M_2$  is located along the positive  $x$ -axis. Stars are drawn from a spherical isotropic distribution bound to  $M_1$ . The problem is completely defined by ten variables:

1. the binary mass ratio  $q \equiv M_2/M_1$ ;
2. the binary eccentricity  $e$ ;
3. the stellar mass  $m_*$ ;
4. the initial distance between the primary hole and the star,  $r_* \equiv |\mathbf{r}_*|$ ;
5. the specific energy of the stellar orbit around  $M_1$ ,  $E_* = -GM_1/(2a_*)$ , or equivalently the semi-major axis of the stellar orbit,  $a_*$ ;
6. the specific angular momentum of the stellar orbit  $L_* = |\mathbf{v} \times \mathbf{r}_*|$ , where  $v \equiv |\mathbf{v}|$  is the stellar velocity relative to  $M_1$ ;
7. four angles:  $\theta$  and  $\phi$  describing the latitude and longitude of the star,  $\psi$  defining the orientation of  $v_\perp$  (the stellar velocity component normal to  $\mathbf{r}_*$ ) i.e. selecting the orbital plane of the star, and  $\Psi$  the initial binary phase.

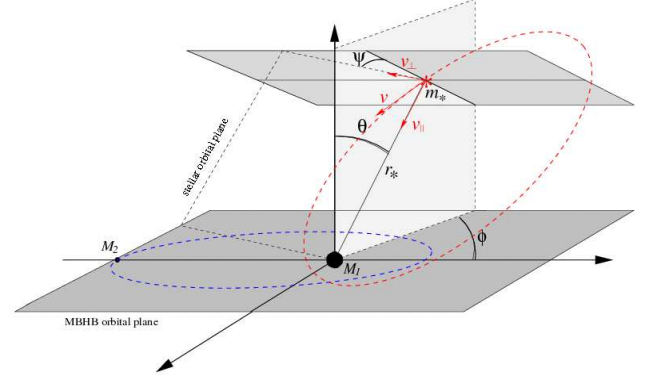


FIG. 1.— Geometry of the three-body scattering experiments. The stellar orbits is determined by  $E_*$  and  $L_*$ , while its orientation with respect to the binary plane is determined by angle  $\psi$ . See text for definition of all symbols.

Compared to the unbound scattering problem (which is defined by nine variables, see Paper I), there is here the extra variable  $r_*$ , and  $E_*$  and  $L_*$  replace the asymptotic initial speed and impact parameter of the incoming field star. A sketch of the experiment set-up is given in Figure 1. In each numerical integration, the binary mass  $M = M_1 + M_2$  and separation  $a$  are set equal to unity, and the stellar mass to  $m_* = 10^{-6}M$ . Scattering events are simulated in sets of  $5 \times 10^4$  trials for fixed values of  $q$  and  $e$ . We sample five values of the binary eccentricity,  $e = 0, 0.1, 0.3, 0.6, 0.9$ , and five values of the binary mass ratio,  $q = 1/9, 1/27, 1/81, 1/243, 1/729$ , for a grand total of 25 models. The distribution of stars bound to  $M_1$  is modeled as follows. The stellar semi-major axis  $a_*$  is randomly sampled from fifty logarithmic bins spanning the range  $0.03a < a_* < 10a$ . The angular momentum is sampled in the interval  $[0, L_{*,\text{max}}^2]$  according to an equal probability distribution in  $L_*^2$ , where  $L_{*,\text{max}}^2 = GM_1 a_*$  is the specific angular momentum of a circular orbit of radius  $a_*$ . A population of stars with such distribution in  $L_*^2$  has mean eccentricity  $\langle e_* \rangle = 0.66$ , corresponding to  $\langle v_\perp \rangle = 2\langle v_\parallel \rangle$ . This condition defines an isotropic stellar distribution (e.g. Quinlan, Hernquist, & Sigurdsson 1995).

The quantities  $E_*$  and  $L_*$  define the shape of the stellar orbit. We sample the initial value of  $r_*$  from the distribution  $\mathcal{P}(r_*)dr_*$ ,

$$\mathcal{P}(r_*)dr_* = \frac{2|E_*|^{3/2}dr_*}{\pi GM_1 \sqrt{E_* - \frac{L_*^2}{2r_*^2} + \frac{GM_1}{r_*}}}, \quad (1)$$

which is proportional to the the fraction of time spent by the star at distance between  $r_*$  and  $r_* + dr_*$  from  $M_1$ . The probability  $\mathcal{P}(r_*)$  is defined in the range  $r_{*,-} < r_* < r_{*,+}$ , where

$$\begin{cases} r_{*,-} = L_*^2 / (GM_1 + \sqrt{G^2 M_1^2 + 2E_* L_*^2}) \\ r_{*,+} = L_*^2 / (GM_1 - \sqrt{G^2 M_1^2 + 2E_* L_*^2}). \end{cases} \quad (2)$$

The angles  $\theta$  and  $\phi$  are randomly generated to reproduce a uniform density distribution over a spherical surface centered on  $M_1$ , while the orientation angle  $\psi$  is chosen from

a uniform distribution in the range  $[0, 2\pi]$ . We start numerical integration with  $M_2$  at its apoastron ( $\Psi = 0$ ), and have checked that the chosen initial phase of the binary does not affect our results. The orbit of the pair is in the  $x - y$  plane with the center of mass at coordinates  $(0, 0, 0)$ .

The nine coupled, second order, differential equations of the three-body problem are integrated using the most recent version of the subroutine DOPRI5, based on an explicit Runge-Kutta method of order 4(5) due to Dormand & Prince (1978). A complete description of the integrator can be found in Hairer, Norsett, & Wanner (1993). The integration is stopped if any of these events occurs:

- the star leaves the sphere of radius  $r = [10^{10}\mu/M]^{1/4}a_0$  with positive total energy, where  $\mu = M_1M_2/M$  is the reduced mass of the binary and  $a_0$  its initial semi-major axis. At  $r$  the force induced by the quadrupole moment of the binary is 10 orders of magnitude smaller than the total force acting on the star at a distance  $a_0$ ;
- the physical integration time exceeds 1 Gyr;
- the integration reaches  $10^8$  time steps. This typically corresponds to the complete integration of  $10^4 - 10^5$  binary orbits.

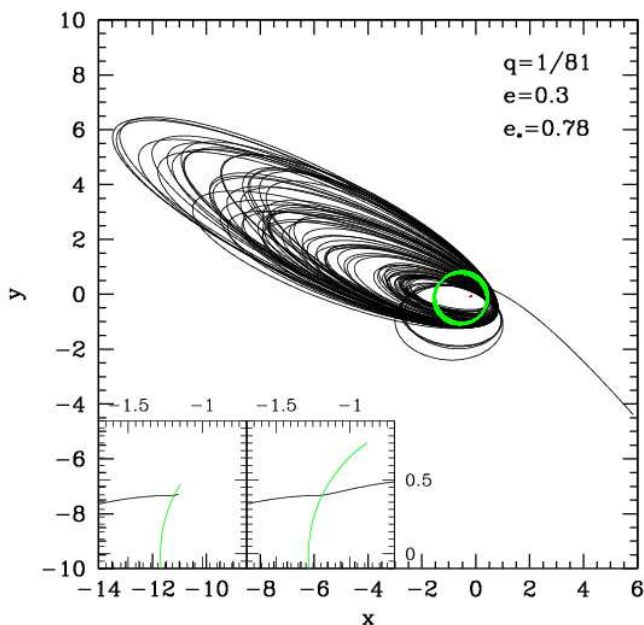


FIG. 2.— Example of a strong three-body interaction unbinding the star. The parameters of the system are listed in the figure. The star is ejected towards the lower right with a kick velocity  $V \approx 0.05V_c$ . The thick circle marks the orbit of  $M_2$ , while the small central dot marks the location of  $M_1$ . The insets zoom-in at the moment of the scattering between the star (approaching from the left) and  $M_2$  (approaching from below).

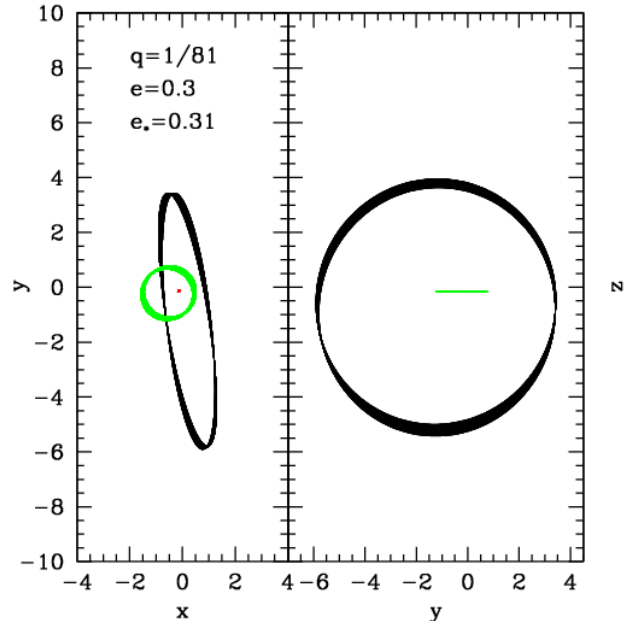


FIG. 3.— Example of a weak three-body interaction. *Left panel:* projection onto the binary  $(x - y)$  plane. *Right panel:* projection onto the  $y - z$  plane.

Examples of integrated stellar orbits are given in Figures 2 and 3. Figure 2 shows a strong interaction: the star has a close encounter with  $M_2$  and leaves the binary sphere of influence with positive energy. Depending on the value of  $a_*$  we have a variable number of numerically “abandoned events”, i.e., bound triple systems that do not readily produce an ejection. Figure 3 shows one of such events: the periastron of the star is much larger than the binary orbital separation  $a$ , and the star is not perturbed by the binary quadrupole field, except for the precession of its periastron.

## 2.2. Tests

We have performed a number of tests to check the sensitivity of our results on numerics. Because of the intrinsically chaotic nature of the three-body problem, the properties of the ejected stars are meaningful only for a statistically-significant sample. The integration of the full three-body problem allows us to directly control the conservation of total energy and angular momentum. The code adjusts the integration stepsize to keep the fractional error per step in position and velocity,  $\epsilon$ , below  $10^{-13}$ . This allows a total energy conservation accuracy of  $\Delta E/E \sim 10^{-9}$  in a single orbit integration, i.e. for  $m_*/M \simeq 10^{-6}$  the energy of the star is conserved at level of one part in a thousand during a single orbit. We varied  $\epsilon$  between  $10^{-11}$  and  $10^{-15}$  and  $m_*/M$  between  $10^{-5}$  and  $10^{-7}$ , and found no significant differences in the statistics of the ejected population. We have also checked that the mean energy and angular momentum exchanges scale linearly with  $m_*$ . A set of longer orbit integrations was performed to test that the number of abandoned events does not depend on the finite numbers of timesteps allowed, again finding no systematic decrease in such a number.

### 2.3. Outputs

Each logarithmic bin in  $a_*$  was sampled by  $10^3$  stars. We calculated the mean energy and angular momentum exchange between the MBHB and the stars, the final velocity and angular distribution of the scattered stars, the fraction  $f_{\text{ej}}$  of stars that are ejected in the interaction, and the ejection timescales. The fraction  $f_{\text{ej}}$  is plotted versus  $a_*/a$  in Figure 4 for different values of the binary parameters  $q$  and  $e$ . Eccentric binaries can eject stars that are initially very tightly bound to  $M_1$ , i.e. with  $a_*$  as small as  $0.1a$ . For  $a_* \gtrsim 3a$ , the expelled fraction declines significantly, regardless of binary eccentricity. It is also evident that the ejection process is more efficient for large values of  $q$ .

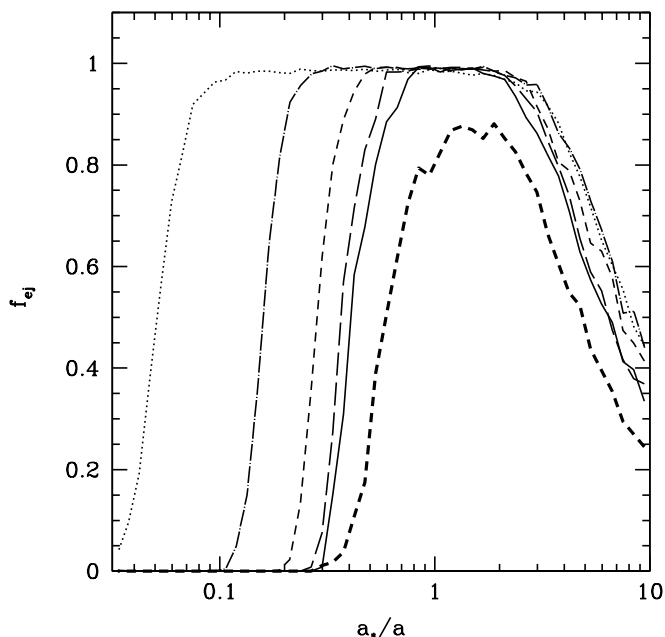


FIG. 4.— Fraction of stars ejected in the interaction as a function of  $a_*/a$ . Thin curves are for  $q = 1/9$  and different eccentricities:  $e = 0$  (solid line),  $e = 0.1$  (long-dashed line),  $e = 0.3$  (short-dashed line),  $e = 0.6$  (dot-dashed line),  $e = 0.9$  (dotted line). The thick dashed line is for  $q = 1/729$  and  $e = 0.3$ .

Figure 5 shows the mean fractional eccentricity change of the pair after each scattering,  $\langle \Delta e/e \rangle$ , as a function of  $a_*/a$ . This quantity is found to scale linearly with  $m_*/M$ . Stars with  $a_* < a$  typically tend to reduce the binary eccentricity, while stars with  $a_* > a$  work in the opposite direction. An eccentric binary spends most of its period near its apocenter, so in the case  $a_* > a$  the probability of a close star-binary encounter (and subsequent star ejection) is maximal at binary apocenter. In the instantaneous interaction the binary velocity decreases. As close to the apocenter the binary velocity is nearly tangential, the binary is forced onto a more radial orbit. On the contrary, a star with  $a_* < a$  “feels” the secondary hole  $M_2$  when it approaches the primary  $M_1$  at a distance  $\sim a_*$ . At that point, the interaction with the star is likely to occur far from the pericenter of  $M_2$  where the velocity of the secondary has a large radial component, hence causing circularization. Note that in this case the absolute value

of  $\Delta e$  is larger, according to the factor  $a/a_*$  in equation (9) (see the different positive and negative  $y$ -axis scales in Fig. 5).

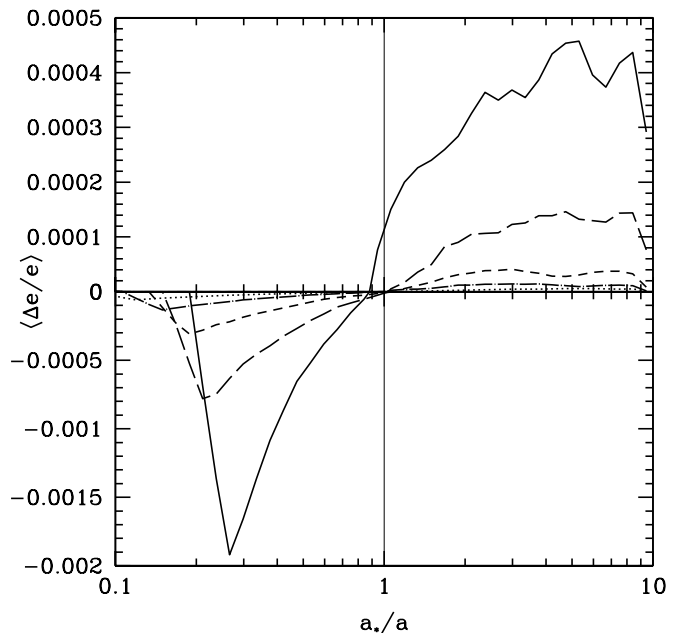


FIG. 5.— Mean fractional eccentricity change,  $\langle \Delta e/e \rangle$ , of the binary after a scattering, as a function of  $a_*/a$ . The assumed initial eccentricity is 0.6, and the different curves are for  $q = 1/729$  (solid line),  $q = 1/243$  (long-dashed line),  $q = 1/81$  (short-dashed line),  $q = 1/27$  (dot-dashed line), and  $q = 1/9$  (dotted line). Note the different scales of the positive and negative  $y$ -axis.

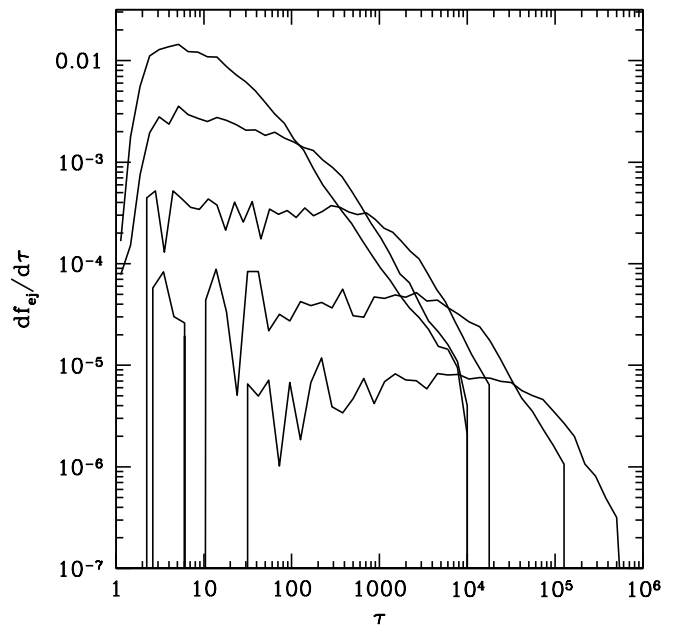


FIG. 6.— Differential distribution of ejection timescales  $\tau$ . The assumed initial eccentricity is 0.3, and the different curves, from top to bottom, are for  $q = 1/9, 1/27, 1/81, 1/243$ , and  $1/729$ .

Figure 6 depicts the fractional number of stars ejected in the time interval  $\tau$  and  $\tau + d\tau$  as a function of the ejection timescale  $\tau$ . The latter is measured in units of the binary orbital period at separation  $a_0 \equiv a(t=0)$ ,  $P_0 = 2\pi\sqrt{a_0^3/(GM)}$ , and is defined as the time elapsed from the start of numerical integration to the moment the interacting star reaches, with positive energy, a distance  $\gg a$  from the binary center-of-mass. For large values of  $q$ , it typically takes the MBHB just a few orbits to expel the star, while lowering  $q$  makes the distribution of slingshot timescales broader and flatter. The ejection rate remains approximatively constant, or decreases slowly, for  $\tau \lesssim 5/q^2$ , and drops dramatically afterwards. Eccentricity plays no role in all the tested cases.

From our scattering experiments, we can finally derive the bivariate distribution functions  $h_1(V, \theta|a_*)$  and  $h_1(V, \phi|a_*)$ , along the same line described in Paper II. For a given  $a_*$ , we record the number of stars with ejection speed in the interval  $V, V + dV$ , leaving the binary with latitude (longitude) at infinity in the interval  $\theta, \theta + d\theta$  ( $\phi, \phi + d\phi$ ). The differential distributions are normalized as follows:

$$\int_0^\infty dV \int_0^\pi d\theta h_1(V, \theta|a_*) = \int_0^\infty dV \int_0^{2\pi} d\phi h_1(V, \phi|a_*) = 1. \quad (3)$$

The subscript “1” is meant to indicate that the scattering experiments are performed for a binary at separation  $a = 1$ .

### 3. HYBRID MODEL OF BINARY DYNAMICS

To study the impact of the gravitational slingshot on the dynamical evolution of a MBHB, we have developed a self-consistent hybrid model, in which numerical results of scattering experiments in a fixed stellar background are coupled to an analytical formulation of loss-cone depletion. This technique allows us to simultaneously follow the orbital decay of the pair as well as the time evolution of the stellar cusp. The hybrid model is similar, in spirit, to the case extensively discussed in Paper II of an unbound stellar population interacting with a black hole pair. Scattering experiments are performed for a binary at fixed orbital separation  $a$ , and the results scaled to any value of  $a$ . Then, by specifying the pace at which  $a$  evolves, we can solve for the binary orbital decay with time. Mathematical details, however, are different from the scheme developed in Paper II. In the unbound case, the pair interacts with a stellar population approaching its sphere of influence at a given rate, and the typical three-body interaction is a “fast” process. For stars bound to  $M_1$  instead, the interacting stellar population is in place from the beginning. The temporal evolution of the system is then determined by the ejection timescale rather than by supply rate.

It is convenient to describe the stellar cusp using  $dN_*/da_*$ , the differential number of stars orbiting  $M_1$  with semi-major axis in the range  $a_*, a_* + da_*$ . For an isotropic stellar distribution

$$\frac{dN_*}{da_*} = C 4\pi a_*^2 \rho(r = a_*), \quad (4)$$

where the stellar density profile is

$$\rho(r) = \rho_0 \left( \frac{r}{r_0} \right)^{-\gamma}, \quad (5)$$

and  $C$  is a fudge factor that depends on the cusp slope,  $C = (1.013, 0.872, 0.831)$  for  $\gamma = (2, 1.75, 1.5)$  (Ivanov, Polnarev, & Saha 2005). Two differential equations determine the rate of change of orbital separation and eccentricity:

$$\frac{da}{dt} = -\frac{2a^2}{GM_1 M_2} \int_0^\infty \Delta\mathcal{E} \frac{d^2 N_{\text{ej}}}{da_* dt} da_*, \quad (6)$$

and

$$\frac{de}{dt} = \int_0^\infty \Delta e \frac{d^2 N_{\text{ej}}}{da_* dt} da_*. \quad (7)$$

We start numerical integration at time  $t = 0$ , orbital separation  $a_0$ , and binary eccentricity  $e_0$ . The terms  $\Delta e$ ,  $\Delta\mathcal{E}$ , and  $d^2 N_{\text{ej}}/da_* dt$  are measured from our scattering experiments. The scaling of the eccentricity change with binary parameters  $m_*/M$ ,  $e$ ,  $q$ , and  $a/a_*$  can be understood from the expression (Quinlan 1996)

$$\Delta e = -\frac{(1-e^2)}{2e} \left( \frac{\Delta\mathcal{E}}{\mathcal{E}} + \frac{2\Delta\mathcal{L}_z}{\mathcal{L}_z} \right), \quad (8)$$

where  $\mathcal{L} = \mu\sqrt{GMa(1-e^2)}$  and  $\mathcal{E} = GM_1 M_2 / (2a)$  are the total angular momentum and energy of the binary. As  $\Delta\mathcal{E} = -\Delta\mathcal{E}_* \sim GM_1 m_*/(2a_*)$  and  $\Delta\mathcal{L}_z = -\Delta\mathcal{L}_* \sim m_*\sqrt{GMa_*}$ , we have  $\Delta\mathcal{E}/\mathcal{E} \sim (m_*/M_2)(a/a_*)$  and  $\Delta\mathcal{L}_z/\mathcal{L}_z \sim (m_*/\mu)\sqrt{a/a_*}$ . It follows then

$$\Delta e \frac{M}{m_*} \propto \frac{(1-e^2)}{e} \frac{a}{a_*} \frac{m_*}{M_2} \frac{M}{m_*} = \frac{(1-e^2)}{e} \frac{a}{a_*} \frac{(1+q)}{q}. \quad (9)$$

The binary energy change per scattering,  $\Delta\mathcal{E}$ , is related to the change of stellar energy  $\Delta\mathcal{E}_*$  by  $\Delta\mathcal{E}_* \simeq -\Delta\mathcal{E}$ , where we have neglected the energy change of the binary center of mass (which is a factor  $m_*/M$  smaller than  $\Delta\mathcal{E}$ ). The quantity  $\Delta\mathcal{E}_*$  can be written as

$$\Delta\mathcal{E}_*(a_*, a, e) = \frac{GM_1 m_*}{2a_*} + \frac{1}{2} k m_* V_c^2(a), \quad (10)$$

where  $V_c(a) = \sqrt{GM/a}$  is the circular velocity of the binary. The numerical factor  $k$  depends upon the ratio  $a_*/a$ , and  $e$ , and is derived from our numerical experiments.

The term  $d^2 N_{\text{ej}}/da_* dt$  quantifies the number of stars orbiting  $M_1$  within  $a_*$  and  $a_* + da_*$  that are ejected from the system in the time interval between  $t$  and  $t + dt$ . This term depends on  $a_*$ ,  $a$ ,  $e$  and  $t$ , and is determined as follows. From scattering experiments we derive the distribution  $P(\tau, s|e)d\tau$  describing the probability that a star at  $s \equiv a_*/a$  becomes unbound from a binary with eccentricity  $e$  in the time interval  $(\tau, \tau + d\tau)$ . Note that the distribution of ejection timescales plotted in Figure 6 is simply the probability function  $P$  averaged over  $s$ ,

$$\frac{df_{\text{ej}}}{d\tau} = \frac{\int P(\tau, s|e) ds}{\int ds}. \quad (11)$$

When  $s \ll 1$  (the exact value depending on  $q$  and  $e$ ) most stars remain bound to  $M_1$ , and  $P = 0$  (see Fig. 4). As  $s \rightarrow 1$  all interacting stars are instead expelled. In the ejection regime the distribution  $P$  is clearly nearly independent on  $s$  and has the same functional form (as

a function of  $\tau$ ) of  $df_{\text{ej}}/d\tau$  (see Fig. 6). From  $P$  we can then compute  $d^2N_{\text{ej}}/da_*dt$  as a function of  $t$  if we set  $\tau = (a_0/a)^{3/2}t$ , where the term  $(a_0/a)^{3/2}$  accounts for the change in the time units of  $P$  as  $a$  changes. Though not formally correct, the scheme catches the basic physics of the interaction in a time-dependent fashion.

Suppose now that in a small time interval  $\Delta t_0$  after the beginning of the interaction the binary remains at constant separation  $a_0$  corresponding to  $s_0 \equiv a_*/a_0$ . The number of stars (with semi-major axis in the interval  $a_*, a_* + da_*$ ) ejected in such time interval is

$$\mathcal{F}_0 \equiv \frac{d^2N_{\text{ej}}}{da_*dt}(0) \Delta t_0 = \frac{dN_*}{da_*} P(0, s_0) \Delta t_0, \quad (12)$$

where for simplicity we have omitted the dependence of  $P$  on the eccentricity. After  $\Delta t_0$  and for an interval  $\Delta t_1$ , the binary settles to a new separation  $a_1$ , corresponding to  $s_1 \equiv a_*/a_1$ . The number of stars ejected in the time interval  $\Delta t_0, \Delta t_0 + \Delta t_1$  is

$$\mathcal{F}_1 = \left( \frac{dN_*}{da_*} - \mathcal{F}_0 \right) \frac{P(\Delta t_0, s_1)}{\int_{\Delta t_0}^{\infty} P(t', s_1) dt'} \Delta t_1 \left( \frac{a_0}{a_1} \right)^{3/2}. \quad (13)$$

The integral at the denominator of the right-hand side renormalizes the distribution  $P$  in the time interval  $[\Delta t_0, \infty]$  so that the correct number of stars is involved. Iterating we have

$$\mathcal{F}_j = \left( \frac{dN_*}{da_*} - \sum_{i=0}^{j-1} \mathcal{F}_i \right) \frac{P(t, s_j)}{\int_t^{\infty} P(t', s_j) dt'} \Delta t_j \left( \frac{a_0}{a_j} \right)^{3/2}, \quad (14)$$

where  $t \equiv \sum_{i=0}^{j-1} \Delta t_i$ . In differential form:

$$\frac{d^2N_{\text{ej}}}{da_*dt}(t) = \left( \frac{dN_*}{da_*} - \int_0^t \frac{d^2N_{\text{ej}}}{da_*dt'} dt' \right) \frac{P(t, s)}{\int_t^{\infty} P(t', s) dt'} \left[ \frac{a_0}{a(t)} \right]^{3/2}, \quad (15)$$

where  $s = s(t) = a_*/a(t)$ . Simultaneous numerical integration of the tree coupled equations (6), (7) and (15) self-consistently solves for the evolution of the binary and the depletion of the stellar cusp.

The bivariate distributions  $h_1(V, \theta|a_*)$  and  $h_1(V, \phi|a_*)$  derived from our suite of scattering experiments (see § 2) can be convolved with the ejection rate  $d^2N_{\text{ej}}/da_*dt$  to compute the final velocity distributions  $h(V, \theta)$  and  $h(V, \phi)$ . The procedure is similar to that described in the Appendix of Paper II. As the binary shrinks to separation  $a < 1$ , the normalized distribution of ejection velocities for stars with semi-major axis in the interval  $a_*, a_* + da_*$  is

$$h_a(V, \theta|a_*) = \frac{1}{\sqrt{a}} h_1 \left( \frac{V}{\sqrt{a}}, \theta|a_* \right), \quad (16)$$

where the ejection speed  $V$  was shifted by the factor  $1/\sqrt{a}$  to account for the increase in the circular velocity of the binary  $V_c$  as the pair shrinks. The prefactor  $1/\sqrt{a}$  normalizes the distribution according to equation (3). The kick velocity function of the expelled population as a whole can then be written as

$$h(V, \theta) = \frac{\int_1^{a_f} \int_0^{\infty} \frac{d^2N_{\text{ej}}}{da_*da} h_a(V, \theta|a_*) da_* da}{\int_1^{a_f} \int_0^{\infty} \int_0^{\pi} \int_0^{\infty} \frac{d^2N_{\text{ej}}}{da_*da} h_a(V, \theta|a_*) da_* da d\theta dV}, \quad (17)$$

where  $a_f$  is the final binary separation,

$$\frac{d^2N_{\text{ej}}}{da_*da} \equiv \frac{d^2N_{\text{ej}}}{da_*dt} \frac{dt}{da}, \quad (18)$$

and  $dt/da$  is given by equation (6). The distribution  $h_1(V, \theta|a_*)$  is evaluated for different values of the eccentricity  $e$ . We can account then for the evolution of binary eccentricity by interpolating the  $h_1$  distribution on a grid of  $e$ -values as the orbit decays. The above procedure returns the velocity distribution in units of  $V_c(a_0)$ . The calculation of  $h(V, \phi)$  can be performed following the same lines.

Finally, integrating the rate  $d^2N_{\text{ej}}/da_*dt$  over the entire evolutionary history of the binary yields the quantity  $dN_{\text{ej}}/da_*$ , which can be compared to  $dN/da_*$  to study the depletion of the stellar cusp by three-body interactions. The Monte Carlo technique developed to address this point is described in § 5.1. The functions  $dN_{\text{ej}}/da_*$  and  $h(V, \theta)$  can be used to check energy conservation, by simply equating the total energy gained by the stars to the increment in the binding energy of the black hole pair, i.e.

$$m_* \int_0^{\infty} \frac{dN_{\text{ej}}}{da_*} \Phi(a_*) da_* + \frac{1}{2} m_* \int_0^{\infty} V^2 N_{\text{ej}} h(V) dV = \frac{GM_1 M_2}{2} \left( \frac{1}{a_f} - \frac{1}{a_0} \right), \quad (19)$$

where  $\Phi(a_*) = GM_1/a_*$ ,  $h(V) = \int h(V, \theta) d\theta$ , and  $N_{\text{ej}} = \int (dN_{\text{ej}}/da_*) da_*$ . We have checked that energy is conserved to better than  $\sim 1\%$ .

It is important to remark at this point that equations (6) and (7) are independent of the absolute value of  $M$  and  $m_*$ . Indeed, in equation (6), the total number of interacting stars is  $\propto M_2/m_*$ , and the energy exchange term is  $\propto M m_*$ . The scaling factor  $1/M_1 M_2$  cancels out, so that the orbital evolution depends only on  $q$  and  $e$ . The same consideration holds for equation (7): as  $\Delta e \propto m_*/M$  while the number of interacting stars  $\propto M_2/m_*$ , the dependence on  $M$  and  $m_*$  cancels out.

#### 4. BINARY EVOLUTION

For comparison with our previous results on the scattering of unbound stars (Paper II), it is convenient to introduce the stellar velocity dispersion  $\sigma$ , and model the *outer* stellar component as a singular isothermal sphere (SIS) with density profile

$$\rho(r) = \frac{\sigma^2}{2\pi G r^2}. \quad (20)$$

We assume that this profile extends inward up to the characteristic radius  $r_0$  within which the total stellar mass is  $2M_1$  (Merritt 2004). Matching the inner cusp described by equation (5) to the outer SIS at  $r_0$  yields

$$r_0 = (3 - \gamma) \frac{GM_1}{\sigma^2}. \quad (21)$$

We also assume that stellar-binary interactions start at separation  $a_0$  where the enclosed mass stellar is  $M_*( < a_0) = 2M_2$ , yielding

$$a_0 = \left( \frac{q}{1+q} \right)^{1/(3-\gamma)} \left[ (3 - \gamma) \frac{GM}{\sigma^2} \right]. \quad (22)$$

This assumption is motivated by recent N-body simulations of the hardening of unequal MBHB in stellar cusps. Matsubayashi, Makino, & Ebisuzaki (2007) found that dynamical friction is efficient in driving orbital decay only as long as the stellar mass inside the binary semi-major axis is  $\gtrsim M_2$ . Beyond this point, the evolution of the pair is driven by three-body interactions with individual stars.

#### 4.1. Orbital evolution and eccentricity growth

Our results on binary orbital decay are summarized in Table 1. A MBHB can shrink by factors ranging from 6 to 18 depending on  $q$ ,  $e_0$ , and  $\gamma$ . The decay factor  $a_0/a_f$  grows with  $e_0$ , as more eccentric binaries can expel stars that are more tightly bound (see Fig. 4). The importance of the initial eccentricity  $e_0$  is modest for low values of  $\gamma$ , since in shallow cusps the number of tightly bound stars is small anyway. The factor  $a_0/a_f$  is also a weakly increasing function of  $q$ , as for higher  $q$  the radius of influence of the binary is larger (in terms of  $a_*/a$ , see Fig. 4). The dependence of the decay factor on  $\gamma$  simply reflects the fact that, for steeper stellar cusps, the mean binding energy of the stars is larger. Note that we have not included the effect of “returning stars” on the decay of the binary. These are ejected stars that do not escape the host bulge, return on small impact parameter orbits, and can have a secondary super-elastic interaction with the MBHB. The role of secondary slingshots was analyzed in Paper II, where it was found that they can boost orbital decay by as much as a factor of 2 for nearly equal-mass binaries, but do not contribute significantly (less than 20% for  $q = 1/9$  and less than 5% for  $q = 1/81$ , see Table 1 of Paper II) to binary hardening for very unequal-mass pairs. In the bound case, the effect of returning stars is likely to be even smaller. Consider for example the case of an isothermal stellar profile: the impact of secondary slingshots is proportional to the number of stars that can interact with the MBHB more than once, i.e. to the size of the loss-cone after the first interaction. For bound stars this is at least a factor of  $\sim 2$  smaller than in the unbound case: so even for  $q = 1/9$ , returning stars would cause at most a  $\sim 10\%$  increase in binary hardening.

Binary eccentricity also grows as a function of  $q$  and  $\gamma$ . A shallow cusp increases the relative importance of stars with large  $a_*$ , and the eccentricity growth is then larger. Moreover, binaries with large  $q$  are more effective in ejecting stars with  $a_*/a \ll 1$ . As these stars act to circularize the binary orbit, nearly equal-mass binaries decay following less eccentric orbits. Figure 7 shows examples of binary evolution as a function of time. Note the different scale of the time axis for the three mass ratios: as shown in Figure 6, it takes nearly equal-mass pairs a smaller number of binary orbits to unbind the stellar cusp. Compared to the scattering of unbound stars, the binary eccentricity grows to larger values because of the stronger average interaction required to expel a bound objects. Results for the  $\gamma = 2$  cusp can also be compared to those obtained in Paper II for the case of a binary interacting with a population of unbound stars. (In Paper II, shrinking factors were normalized to the “hardening radius”  $a_h \equiv GM_2/4\sigma^2$ , where, by definition,  $a_0 = 4a_h$  for  $\gamma = 2$ .) Binaries with  $e_0 = 0.1$  and  $q = (1/9, 1/27, 1/81, 1/243)$ , for example, shrink by the factors  $a_h/a_f = (2.09, 2.55, 2.35, 2.33)$  according to Table 1, compared to the corresponding

$a_h/a_f = (2.09, 1.49, 1.19, 1.06)$  for the unbound case, i.e. very unequal-mass binaries can only decay by extracting the cusp binding energy. The evolution of the eccentricity in the bound and unbound cases is compared in Figure 8, for two different initial values of  $e_0$ . The three-body scattering of bound stars clearly leads to a significant increase of binary eccentricity.

$q$	$e_0$	$\gamma = 1.5$		$\gamma = 1.75$		$\gamma = 2$	
		$a_0/a_f$	$e_f$	$a_0/a_f$	$e_f$	$a_0/a_f$	$e_f$
$1/9$	0.1	9.63	0.608	9.89	0.350	11.38	0.179
	0.5	9.99	0.972	11.55	0.907	15.77	0.753
	0.9	10.06	0.998	11.80	0.992	17.73	0.969
$1/27$	0.1	8.06	0.691	8.35	0.532	10.19	0.408
	0.5	8.26	0.959	9.35	0.862	12.35	0.710
	0.9	8.27	0.996	9.64	0.988	14.03	0.958
$1/81$	0.1	6.99	0.755	7.75	0.650	9.39	0.542
	0.5	6.90	0.922	7.81	0.828	10.14	0.717
	0.9	6.89	0.996	7.81	0.974	11.00	0.937
$1/243$	0.1	6.49	0.906	7.28	0.805	9.30	0.688
	0.5	6.39	0.971	7.25	0.914	9.92	0.818
	0.9	6.38	0.962	7.19	0.986	10.09	0.955
$1/729$	0.1	6.12	0.881	6.91	0.814	8.94	0.724
	0.5	5.95	0.919	6.91	0.869	9.09	0.797
	0.9	5.94	0.977	6.92	0.953	9.41	0.900

TABLE 1  
Binary shrinking factors and final eccentricities from the hybrid model.

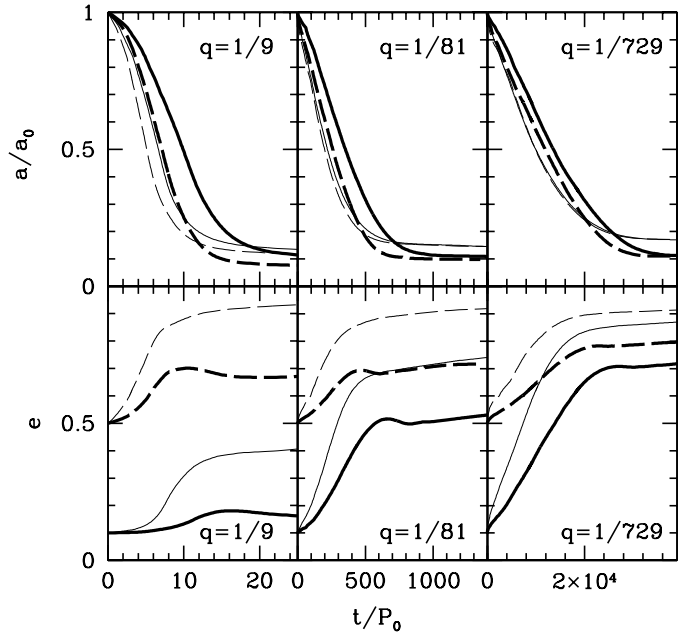


FIG. 7.— Time evolution of the binary semi-major axis (upper panels) and eccentricity (lower panels). Left panels:  $q = 1/9$ . Central panels:  $q = 1/81$ . Right panels:  $q = 1/729$ . In all panels the thick lines are for a  $\gamma = 2$  stellar cusp, while the thin lines are for  $\gamma = 1.5$ . The initial binary eccentricity is assumed to be 0.1 (solid lines) and 0.5 (dashed lines).



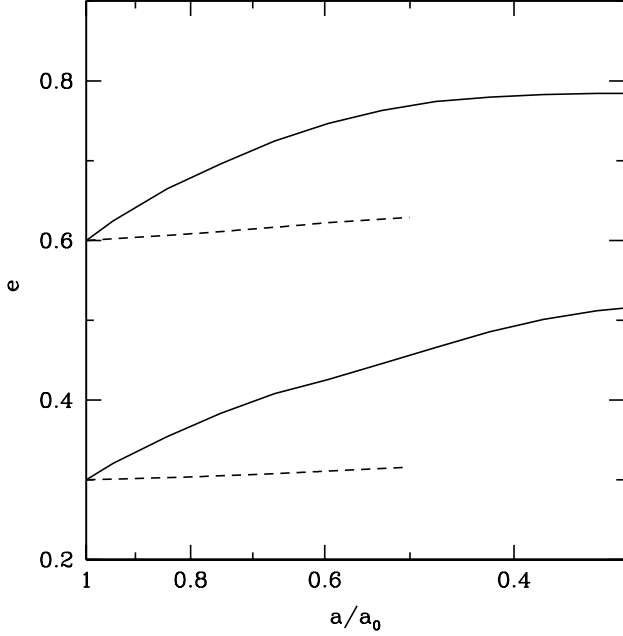


FIG. 8.— Evolution of binary eccentricity as a function of orbital separation, for the case of interactions with unbound stars (Paper I II, *dashed lines*), and with a bound cusp (*solid lines*). The binary is embedded in an SIS, its mass ratio is  $q = 1/9$ , and its initial eccentricity is  $e_0 = 0.3$  and  $0.6$ . Note that the scattering experiments with bound stars start at  $a_0 = a_h$ , while those with bound stars start at  $a_0 = 4a_h$  (see text for details).

#### 4.2. Final coalescence

Consider now, as in Paper II, the separation at which a MBHB can coalesce in less than 1 Gyr because of the emission of gravitational waves (GWs):

$$a_{\text{GW}} \simeq \frac{a_h}{250} \left( \frac{1+q}{q} \right)^{3/4} M_{1,6}^{1/4} F(e)^{1/4}, \quad (23)$$

where  $M_{1,6} \equiv M_1/10^6 M_\odot$  and, to 4th order in  $e$ ,

$$F(e) \equiv (1 - e^2)^{-7/2} \left( 1 + \frac{73}{24}e^2 + \frac{37}{96}e^4 \right) \quad (24)$$

(Peters 1964). Assuming as before that three-body interactions begin operating at separation  $a_0$ , and combining equations (22) and (23), we get

$$\frac{a_f}{a_{\text{GW}}} \simeq 10^3 \frac{a_f}{a_0} (3-\gamma) \left( \frac{q}{1+q} \right)^{(1+\gamma)/(12-4\gamma)} M_{1,6}^{-1/4} F(e)^{-1/4}. \quad (25)$$

If  $a_f/a_{\text{GW}} < 1$ , then a MBHB would coalesce in less than 1 Gyr after interaction with a bound stellar cusp. As shown in the “coalescence diagram” of Figure 9, eccentric, massive, very unequal-mass binaries embedded in steep stellar cusps are favored to reach coalescence. The steeper the cusp, the wider the portion of the  $M_1 - q$  plane where coalescence can be reached within 1 Gyr.

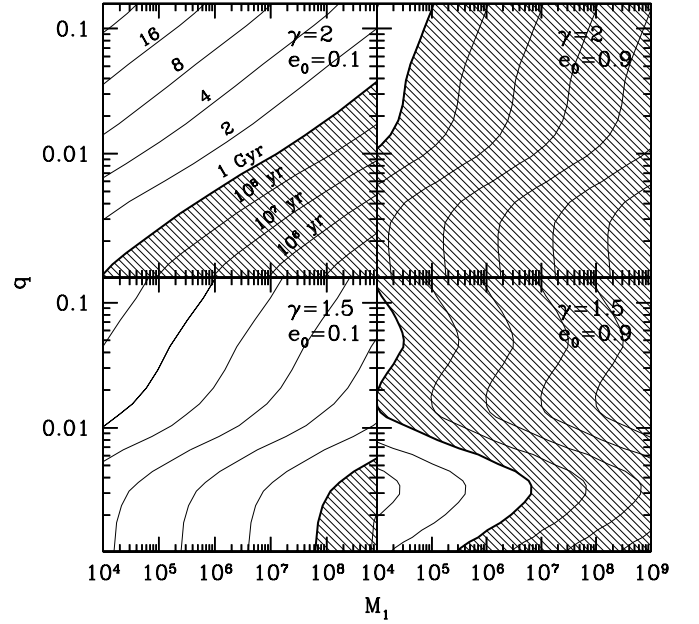


FIG. 9.— Coalescence diagram. In each panel, the *thick line* delimits those MBHBs that can coalesce, because of GW emission, in less than 1 Gyr starting from separation  $a_f$  (*shaded area*). As shown in the upper left panel, level curves to the left of such line are labelled according to the ratio  $a_f/a_{\text{GW}}$  reached by the binary at the end of the shrinking process (equation 25), while level curves to the right are labelled according to the coalescence time at  $a_f$ .

### 5. EVOLUTION OF THE STELLAR CUSP

#### 5.1. Cusp erosion

The orbital decay of the pair occurs following the ejection of a mass  $\sim 2 - 4 M_2$  (depending on cusp slope and binary eccentricity) and results in the progressive erosion of the stellar cusp. Eccentric binaries can shrink rapidly by scattering at pericenter a fewer number of deeply bound stars. More mass is expelled in the case of shallower cusps, because of the larger number of stars surrounding the binary just outside  $a_0$ . The hybrid approach allows us to compute the binary-driven evolution of the stellar density profile *a posteriori*. Self-consistent integration of the orbital decay yields  $dN_{\text{ej}}/da_*$ , and the number of stars that remain bound to  $M_1$  as a function of  $a_*$  is simply

$$\frac{dN_{\text{bd}}}{da_*} = \frac{dN_*}{da_*} - \frac{dN_{\text{ej}}}{da_*}. \quad (26)$$

We assume that the stellar cusp remains isotropic, i.e.  $\langle e_* \rangle = 0.667$ . The  $a_*$  domain is then subdivided in intervals  $\Delta a_*$ , and for each interval a number of bound stars  $\propto (dN_{\text{bd}}/da_*)\Delta a_*$  is generated with angular momentum distribution  $\propto L_*^2$ . We then compute the probability of finding a star at distance between  $r$  and  $r + dr$  from  $M_1$  (this is proportional to the time spent at such distance along its orbit), and reconstruct the stellar density profile  $\rho(r)$ . Figure 10 shows the profile before and after binary shrinking. The cusp is eroded between  $\sim 0.01a_0$  and  $\sim 2a_0$ , depending on  $e_0$ . For  $r \lesssim a_0$ , a SIS is flattened to  $\rho \propto r^{-0.7}$ , while a  $r^{-1.5}$  cusp becomes  $\rho(r) \propto r^{-0.5}$ . Such results are independent of the mass ratio  $q$ . As three-body



interactions and stellar ejections tend to circularize the orbits of ambient stars, one may wonder about the validity of the assumption that the cusp remains isotropic. We find that the assumed mean eccentricity of the remaining bound population can modify the cusp slope by a factor  $\simeq 0.3$ . Therefore, depending on  $\gamma$  and on the final anisotropy of the remaining stars, the stellar cusps will be flattened to  $\rho(r) \propto r^{-0.3} - r^{-0.8}$  by the shrinking MBHB.

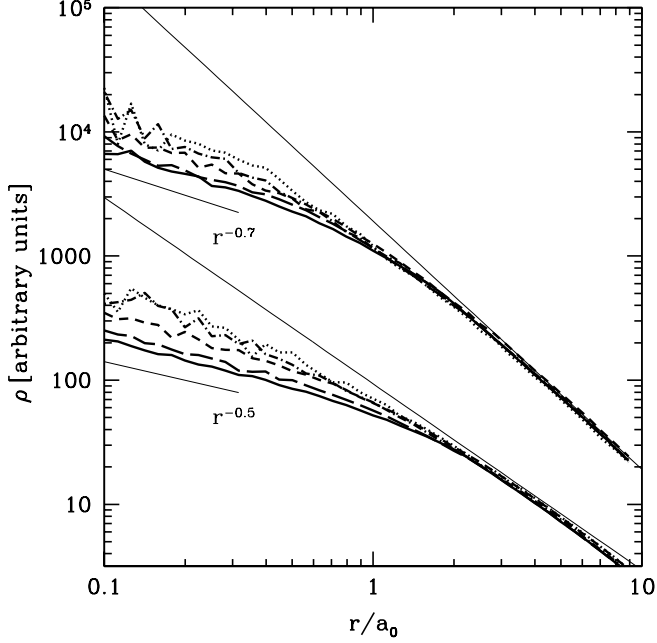


FIG. 10.— The cusp stellar density profiles (in arbitrary units) before (*thin lines*) and after (*thick lines*) erosion by the shrinking binary. *Solid line*:  $q = 1/9$ ; *Long-dashed line*:  $q = 1/27$ ; *Short-dashed line*:  $q = 1/81$ ; *Dot-dashed line*:  $q = 1/243$ ; *Dotted line*:  $q = 1/729$ . The upper (lower) set of curves is for  $\gamma = 2$  ( $\gamma = 1.5$ ). Fiducial  $r^{-0.7}$  and  $r^{-0.5}$  power-laws are shown for reference.

### 5.2. Distribution of kick velocities

The distribution of stellar ejection velocities in units of the binary circular velocity at the initial separation  $a_0$ ,  $V_{c,0}$ , is shown in Figure 11. The distribution cannot be fit by a single or a broken power-law, as in the case of the kick velocities imparted at fixed binary given separation, as the derivative of the distribution is a monotonic decreasing function of the ejection speed. While the peak of the distribution shifts toward smaller  $V/V_{c,0}$  values as  $q$  decreases ( $V_{\text{peak}} \propto \sqrt{q}$ ), the high velocity tail is independent of  $q$ . For initially eccentric binaries, the velocity of  $M_2$  at periastron is  $> V_{c,0}$  and a significant number of HVSs can then be generated. Note that the speed distribution is only weakly dependent on  $\gamma$  once  $V$  is expressed in units of  $V_{c,0}$ .

### 5.3. Ejected mass

Integration of the kick velocity distribution gives the ejected mass  $M_{\text{ej}}$ . This quantity is plotted in Figure 12 as a function of  $q$  for different lower velocity thresholds. As discussed above, the total number of ejected stars is approximately  $\propto q$  and is weakly dependent on  $e_0$  and  $\gamma$ .

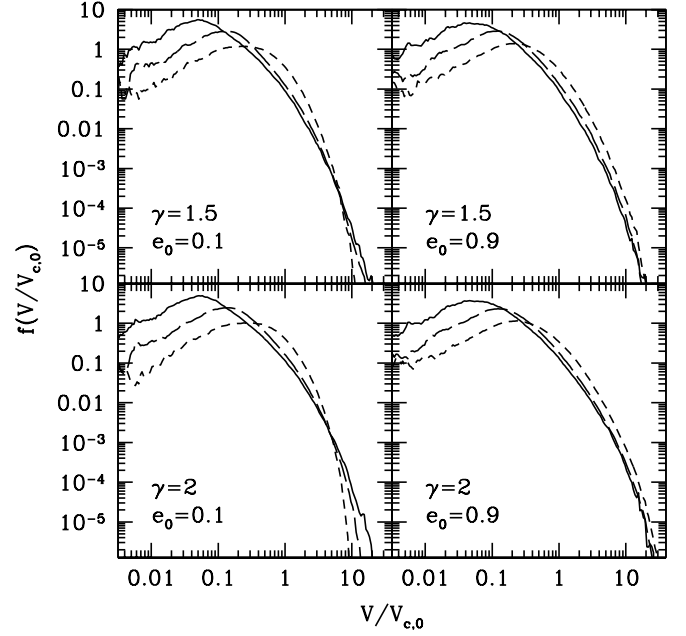


FIG. 11.— Final velocity distribution of ejected stars as a function of  $V/V_{c,0}$ . *Short-dashed lines*:  $q = 1/9$ ; *Long-dashed lines*:  $q = 1/81$ ; *Solid lines*:  $q = 1/729$ . The assumed values of  $\gamma$  and  $e_0$  are listed in each panel.

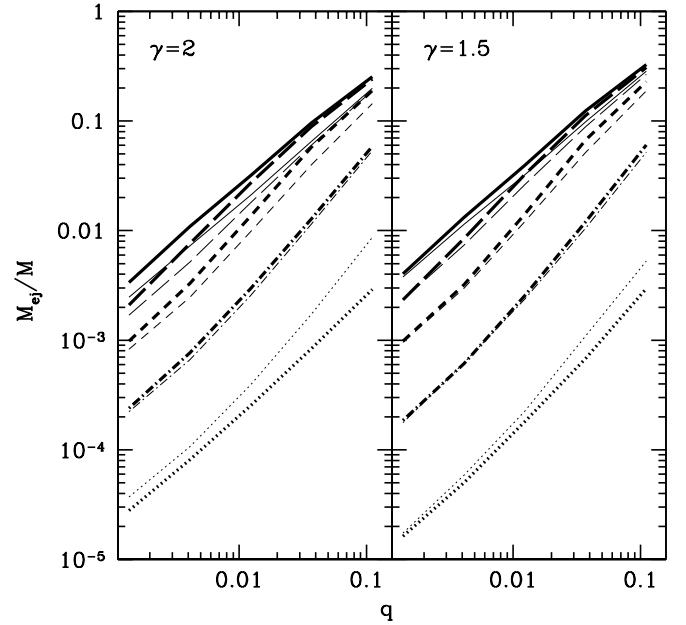


FIG. 12.— Mass ejected from the binary as a function of  $q$ . *Left panel*:  $\gamma = 2$ . *Right panel*:  $\gamma = 1.5$ . *Thick lines*:  $e_0 = 0.1$ . *Thin lines*:  $e_0 = 0.9$ . In each set of curves lines refers, from top to bottom, to all stars with kick velocities  $V > 0$  (the total mass expelled by the binary) and with  $\log(V/V_{c,0}) > -1 + 0.5n$  for  $n = 0, 1, 2, 3$ .

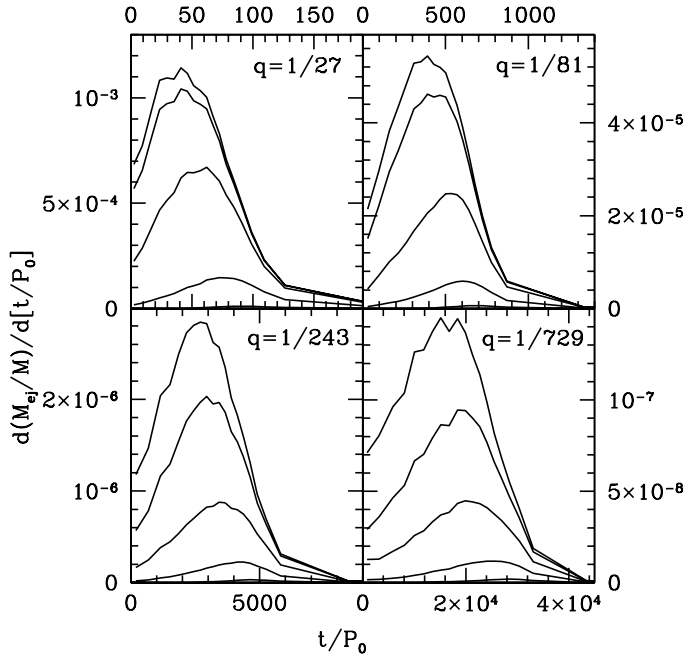


FIG. 13.— Mass ejection rate for binaries with  $e_0 = 0.1$  and different mass ratios embedded in an SIS. Lines refer, from top to bottom, to all stars with kick velocities  $V > 0$  (the total mass expelled by the binary) and with  $\log(V/V_{c,0}) > -1 + 0.5n$  for  $n = 0, 1, 2, 3$ . Note that the time axis has a different scale in each panel.

Moreover, the number of stars ejected above a given velocity threshold (in units of  $V_{c,0}$ ) is also weakly dependent upon these two parameters. Stellar ejection occurs in a burst lasting from few tens to several thousands binary orbital periods (see Fig. 13, note the different scale of the time axis in the four panels), i.e. from  $10^5$  to  $10^7$  yr. The highest velocity stars are delayed with respect to the bulk of ejections, as large kicks require close binary separations. The ejection rate peaks at earlier times in the case of more eccentric binaries, and is larger for steeper cusps.

#### 5.4. Angular properties of HVSs

The angular properties of HVSs show several peculiar features, qualitatively similar to those discussed in Paper I for the scattering of an unbound stellar population. The ejected stars are flattened in the binary orbital plane, and, in the case of eccentric binaries, are grouped into a “broad jet” aligned to the velocity of  $M_2$  at periastron. Both anisotropies are more pronounced in stars undergoing a stronger interaction and receiving larger kicks. The anisotropy of the HVS population can be quantified by computing as a function of binary separation the angles  $\langle\theta^2\rangle$  and  $\langle\phi\rangle$ , where  $-\pi/2 < \theta < \pi/2$  is the latitude of the star (the angle between the velocity vector  $V$  at infinity and the binary orbital plane), and  $0 < \phi < 2\pi$  is its longitude (the angle between the projection onto the binary orbital plane of the velocity vector at infinity and the  $x$ -axis). For a spherically-symmetric distribution,  $\langle\theta^2\rangle \simeq 0.47$ , and  $\langle\phi\rangle = \pi$ . We find  $\langle\theta^2\rangle \sim 0.35 - 0.40$  for all HVSs. As a general trend, stars ejected above a given speed tend to become more isotropic as the binary shrinks, confirming the analytical result of Levin (2006). This effect was already seen in three-body scattering experiments of unbound stars (see Paper I for a detailed discussion), and

is related to the fact that, as the pair decays, its circular velocity grows and even stars experiencing relatively weak encounters can attain large kick velocities. In terms of longitude, HVSs are ejected almost isotropically, though an azimuthal anisotropy become apparent with increasing kick velocities. The high-velocity tail of the distribution is formed by stars expelled after a close encounter with  $M_2$  near its periastron, in a broad jet with  $\langle\phi\rangle \simeq 3/2\pi$ . As the binary potential is non-Keplerian, such broad jet will precess during binary evolution on a timescale that depends upon  $q$  and  $\gamma$  (Levin 2006).

#### 6. THE CASE OF SGR A\*

Most of the results presented in the previous sections are scale invariant, i.e. they are independent on the absolute value of  $M$  and on the chosen normalization of the stellar cusp. The only underlying assumption is that the interaction between the MBHB and ambient stars begins when the stellar mass inside the binary orbit is equal to  $2M_2$ . We are interested in scaling our results to the scattering of stars bound to Sgr A\*, the massive black hole in the Galactic Center, by an inspiraling companion of intermediate mass (Yu & Tremaine 2002; Sesana, Haardt & Madau 2007b). Let us first express equations (20), (21), and (22) in physical units:

$$r_0 = 0.43 \text{ pc } (3 - \gamma) M_{1,6} \sigma_{100}^{-2}, \quad (27)$$

$$\rho_0 = 1.96 \times 10^6 M_\odot \text{ pc}^{-3} (3 - \gamma)^{-2} M_{1,6}^{-2} \sigma_{100}^6, \quad (28)$$

$$a_0 = 0.43 \text{ pc } (3 - \gamma) M_{1,6} \sigma_{100}^{-2} q^{1/(3-\gamma)} (1 + q)^{(2-\gamma)/(3-\gamma)}, \quad (29)$$

where  $\sigma_{100}$  is measured in units of  $100 \text{ km s}^{-1}$ . From  $a_0$ , the time unit of our experiments is then

$$P_0 = 1.3 \times 10^5 \text{ yr } (3 - \gamma)^{3/2} M_{1,6}^{1/4} q \left( \frac{q}{1 + q} \right)^{(2\gamma-3)/(6-2\gamma)}. \quad (30)$$

The stellar density profile around the Galactic Center can be described as a double power-law, with outer slope  $\simeq -2$  and inner slope  $\simeq -1.5$  (Genzel et al. 2003; Schodel et al. 2007). The massive black hole Sgr A\* weighs  $\simeq 3.5 \times 10^6 M_\odot$  (Schodel et al. 2002; Ghez et al. 2005). Using  $M_{1,6} = 3.5$ ,  $\sigma_{100} = 1$  and  $\gamma = 1.5$ , from equations (27) and (28) we obtain  $r_0 = 2.26 \text{ pc}$ , and  $\rho_0 = 7 \times 10^4 M_\odot \text{ pc}^{-3}$ , in good agreement with the most recent observations (Merritt 2006; Schodel et al. 2007). For the relevant values of  $q$  and  $\gamma$ , the typical timescale for orbital decay ranges between  $\sim 10^5$  and  $\sim 10^7$  yrs (see eq. 30). In the following, we will consider two different mass ratios for the putative MBHB at the Galactic Center,  $q = 1/243$  and  $q = 1/729$ , corresponding to an inspiraling IMBH of mass  $M_2 \simeq 1.4 \times 10^4 M_\odot$  and  $M_2 \simeq 4.8 \times 10^3 M_\odot$ , respectively, as well as two different slopes for the initial inner stellar cusp,  $\gamma = 1.5$  and  $\gamma = 1.75$ . We will also study the impact of binary initial eccentricity. The parameters of the different models considered are listed in Table 2.

$\gamma$	$r_0$ [pc]	$\rho_0$ [ $M_\odot \text{ pc}^{-3}$ ]	$q$	$a_0$ [pc]	$P_0$ [yr]	$V_{c,0}$ [ $\text{km s}^{-1}$ ]
1.5	2.25	$7.1 \times 10^4$	1/243	0.058	1344	510
			1/729	0.028	448	735
1.75	1.88	$10^5$	1/243	0.023	340	806
			1/729	0.010	91	1250

TABLE 2

Parameters of two different models for the stellar cusp at the Galactic Center. The quantities  $\gamma$ ,  $r_0$ ,  $\rho_0$ ,  $q$ ,  $a_0$ ,  $P_0$ , and  $V_{c,0}$  are, respectively, the cusp slope, the cusp characteristic radius, the density at  $r_0$ , the binary mass ratio, the binary separation at which gravitational slingshots start, the binary orbital period at  $a_0$ , and the binary circular velocity at  $a_0$ .

The dynamical evolution of a putative IMBH-Sgr A\* binary is displayed in Figure 14 for  $e_0 = 0.1$ . The two upper panels show the time-changing semi-major axis  $a$  and eccentricity  $e$ . The former shrinks to  $10^{-2} - 10^{-3}$  pc in 2-15 Myrs, depending on  $q$  and  $\gamma$ . Lighter IMBHs reach smaller separations on a longer timescale. Our results for the case  $\gamma = 1.75$  can be directly compared to the numerical simulations of Baumgardt et al. (2006) and Matsubayashi et al. (2007), and are found to be in excellent agreement. The eccentricity increases rapidly in all cases to values  $\gtrsim 0.8$ . We have checked that, when  $e_0 > 0.3$ , the binary eccentricity can reach values as large as  $e \gtrsim 0.95$ . This is again in agreement with the results of Baumgardt et al. (2006) and Matsubayashi et al. (2007). In the figure we have marked with an horizontal dotted line the separation at which the binary can coalesce in 1 Gyr because of GW emission (eq. 23). Only for a cusp as steep as  $\gamma = 1.75$  does the pair actually reach such separation. One should note that, while in our hybrid model the eccentricity evolves smoothly, in a realistic situation it will undergo discontinuous “jumps” triggered by rare close encounters, which could induce extreme eccentricities and accelerate coalescence. The two lower panels of Figure 14 show the resulting stellar density profiles after binary erosion. Cusps are flattened to  $\rho \propto r^{-0.7}$  in the central few  $\times 10^{-2}$  pc. The numerical simulations of Baumgardt et al. (2006) and Matsubayashi et al. (2007) produce somewhat shallower slopes, a discrepancy that may be associated with our assumption of an isotropic stellar cusp after the interaction.

The heating of the cusp results in the creation of a population of HVSs. In Figure 15 we plot the stellar ejection rates as a function of time for different models and for different velocities at the radius of influence of Sgr A\*. Modelling the Milky Way potential as the sum of a luminous component (Miyamoto & Nagai 1975) and a dark matter halo (Widrow & Dubinski 2005), we find an escape velocity from the Milky Way of  $\simeq 840 \text{ km s}^{-1}$  at  $r_{\text{inf}}$ . This velocity threshold translates, in such a gravitational potential, into about  $450 \text{ km s}^{-1}$  10 kpc away from Sgr A\*. Stars with  $V > 300 \text{ km s}^{-1}$  at  $r_{\text{inf}}$  do not leave the bulge, while stars with  $V > 600 \text{ km s}^{-1}$  can reach 4 kpc away from the Galactic Center. Stars with  $V > 900 \text{ km s}^{-1}$  and  $V > 1200 \text{ km s}^{-1}$  are not bound to the Milky Way and, at a reference distance of 10 kpc, have still velocities of  $600 \text{ km s}^{-1}$  and  $1000 \text{ km s}^{-1}$ , respectively. Figure 15 shows that the ejection occurs in a relatively short burst lasting a few Myrs, with higher velocity stars being produced at increasingly later times. At peak, the ejection rate of HVSs with  $V > 900 \text{ km s}^{-1}$  varies between  $5 \times 10^{-5}$  and

$2 \times 10^{-3} \text{ yr}^{-1}$ , depending on  $q$  and  $\gamma$ . The rate is larger in steeper cusps, as stars are more centrally concentrated and are scattered when the binary separation is smaller and orbital velocity larger.

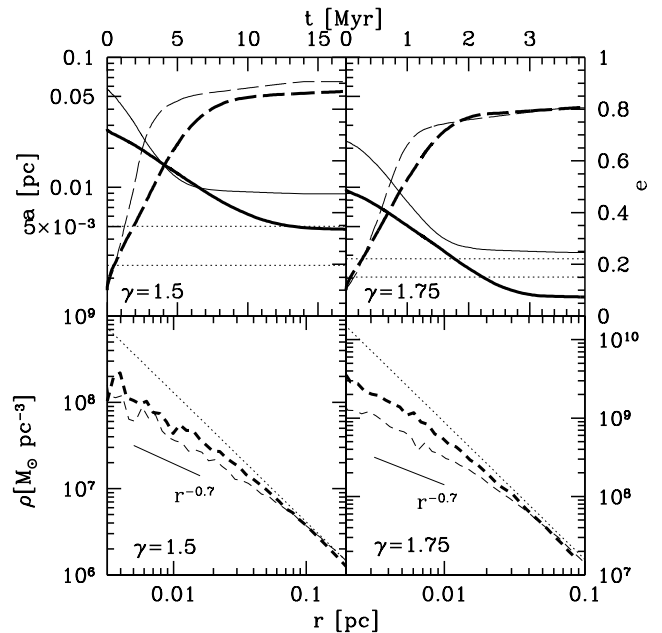


FIG. 14.— The case of Sgr A\*. *Upper panels*: time evolution of binary semi-major axis (solid lines, left axis scale) and eccentricity (dashed-line, right axis scale) for  $e_0 = 0.1$ . The dotted lines mark the separation at which binaries can coalesce because of GW emission in < 1 Gyr. *Lower panels*: evolution of the stellar density profile. In all panels, the thin lines are for  $q = 1/243$ , the thick lines for  $q = 1/729$ .

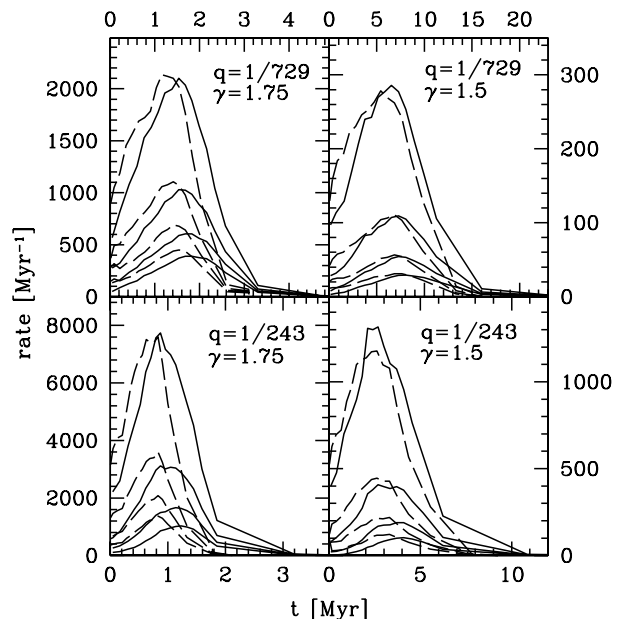


FIG. 15.— Ejection rate of HVSs for an IMBH falling onto Sgr A\*. *Solid lines*:  $e_0 = 0.1$ ; *dashed lines*:  $e_0 = 0.9$ . For each set of curves, lines from top to bottom correspond to a velocity threshold  $V > 300, 600, 900,$  and  $1200 \text{ km s}^{-1}$  at the radius of influence of Sgr A\*, respectively.

The speed distribution of HVSs depends on the details of the model. In the range  $300 - 1000 \text{ km s}^{-1}$  (the velocity range of the HVSs observed by Brown et al. 2006), and at a Galactocentric distance of 55 kpc (the average distance of the observed HVSs), the distribution can be approximated by a power-law  $f(V) \propto V^{-1.5}$ , almost independent of  $q$ ,  $e_0$ , and  $\gamma$ . Assuming  $m_* = 1 M_\odot$ , we find a predicted number of HVSs with  $V > 840 \text{ km s}^{-1}$  at  $r_{\text{inf}}$   $N_{\text{HVS}} \simeq 525$  (1290) for  $q = 1/729$  and  $\gamma = 1.5$  (1.75). This number roughly doubles for  $q = 1/243$  and is fairly independent on  $e_0$ . Our results are consistent with Baumgardt et al. (2006), who estimate  $N_{\text{HVS}} \sim 1700$  for  $M_2 = 10^4 M_\odot$ , and  $N_{\text{HVS}} \sim 900$  for  $M_2 = 3 \times 10^3 M_\odot$ . A peak of ejection occurs after  $\sim 1 - 2 \text{ Myr}$ . Levin (2006) finds comparable numbers of stars expelled, and a similarly peaked ejection rate.

## 7. SUMMARY

We have performed, for the first time, scattering experiments between a MBHB and stars drawn from a cusp bound to the primary hole. We have studied the dynamics of the pair and its orbital decay by three-body interactions, the impact of the gravitational slingshot on the stellar density profile, the properties of the ejected stellar population, and have scaled our results to the case of Sgr A\*. Our results can be quickly summarized as follows:

1. The extraction of the cusp binding energy causes the binary to shrink by a larger factor compared to the scattering of unbound stars. The effect is more noticeable in the case of small mass ratios  $q$ .
2. The binary orbital eccentricity increases much more rapidly compared to the unbound case. The eccentricity growth is more pronounced in small mass-ratio binaries, and for shallower stellar cusps.

3. The combined effects of enhanced orbital decay and eccentricity growth lead very unequal-mass binaries to the gravitational wave coalescence phase. The detailed fate of the pair depends on the absolute value of its mass. More massive binaries decay faster.
4. The stellar cusp is eroded by the slingshot mechanism, and the total mass removed is 2-to-4 times the mass of the secondary. Ejection happens in a “burst” lasting from few tenths to several thousands binary orbital periods, depending upon  $q$ .
5. Scaled to the scattering of stars bound to Sgr A\* by an inspiralling IMBH, our results imply the formation of a core of 0.1 pc in 1-10 Myrs, as well as the ejection of 500-2500 HVSs moving with speeds sufficient to escape the gravitational field of the Milky Way. In Sesana et al. (2007b) we have used the Brown et al. (2007) sample of unbound and bound HVSs together with numerical simulations of the propagation of HVSs in the Milky Way halo to constrain this ejection mechanisms, and shown that it appears to produce a spectrum of ejection velocities that is too flat compared to the observations. Future astrometric (as, e.g., *GAIA*) and deep wide-field (as, e.g., *LSST*) surveys should unambiguously identify the ejection mechanism of HVSs, and probe the Milky Way potential on scales as large as 200 kpc (Gnedin et al. 2005; Yu & Madau 2007).

Support to this work was provided by NASA grant NNG04GK85G (P.M.).

## REFERENCES

- Baumgardt H., Gualandris A., & Portegies Zwart S. 2006, MNRAS, 372, 174  
 Begelman, M. C., Blandford, R. D., & Rees, M. J. 1980, Nature, 287, 307  
 Brown, W. R., Geller, M. J., Kenyon, S. J., & Kurtz, M. J. 2006, ApJ, 647, 303  
 Brown, W. R., Geller, M. J., Kenyon, S. J., Kurtz, M. J., & Bromley, B. C. 2007, ApJ, 660, 311  
 Dormand, J. R., & Prince, P. J. 1978, CeMec, 18, 223  
 Ebisuzaki, T., Makino, J., & Okumura, S. K. 1991, Nature, 354, 212  
 Faber, S. M., et al. 1997, AJ, 114, 1771  
 Genzel, R., et al. 2003, ApJ, 594, 812  
 Ghez, A. M., et al. 2005, ApJ, 620, 744  
 Gnedin, O. Y., Gould, A., Miralda-Escudé, J., & Zentner, A., R. 2005, ApJ, 634, 344  
 Hairer, E., Norsett, S. P., & Wanner, G. 1993, Solving Ordinary Differential Equations I. Nonstiff Problems (Berlin: Springer-Verlag)  
 Hills, J. G. 1988, Natur, 331, 687  
 Ivanov, P. B., Polnarev, A. G., & Saha, P. 2005, MNRAS, 358, 1361  
 Levin, Y. 2006, ApJ, 653, 1203  
 Makino, J., & Ebisuzaki, T. 1996, ApJ, 465, 527  
 Matsubayashi, T., Makino, J., & Ebisuzaki, T. 2007, ApJ, 656, 879  
 Mayer, L., Kazantzidis, S., Madau, P., Colpi, M., Quinn, T., & Wadsley, J. 2007, Science, 316, 1874  
 Merritt, D. 2006, Rept.Prog.Phys., D69, 2513  
 Milosavljevic, M., & Merritt, D. 2001, ApJ, 563, 34  
 Miyamoto, M., & Nagai, R. 1975, PASJ, 27, 533  
 Peters, P. C. 1964, Phys. Rev. B., 136, 1224  
 Quinlan, G. D. 1996, NewA, 1, 35 (Q96)  
 Quinlan, G. D., & Hernquist, L. 1997, NewA, 2, 533  
 Quinlan, G. D., Hernquist, L., & Sigurdsson, S. 1995, ApJ, 440, 554  
 Ravindranath, S., Ho, L. C., Peng, C. Y., Filippenko, A. V., & Sargent, W. L. W. 2001, AJ, 122, 653  
 Schodel, R., et al. 2002, Nature, 419, 694  
 Schodel, R., et al. 2007, A&A, 469, 125  
 Sesana, A., Haardt, F., Madau, P., & Volonteri, M. 2005, ApJ, 623, 23  
 Sesana, A., Haardt, F., & Madau, P. 2006, ApJ, 651, 392 (Paper I)  
 Sesana, A., Haardt, F., & Madau, P. 2007a, ApJ, 651, 392 (Paper II)  
 Sesana, A., Haardt, F., & Madau, P. 2007b, MNRAS, 379, 45  
 Volonteri, M., Haardt, F., & Madau, P. 2003, ApJ, 582, 599  
 Volonteri, M., Madau, P., & Haardt, F. 2003, ApJ, 593, 661  
 Widrow, L. M., & Dubinski, J. 2005, ApJ, 631, 838  
 Yu, Q., & Madau, P. 2007, MNRAS, 379, 1293  
 Yu, Q., & Tremaine, S. 2003, ApJ, 599, 1129